ACS APPLIED ENERGY MATERIALS

www.acsaem.org

Article

Hydrophilicity as a Key Factor in Enhancing Oxygen Evolution Reaction on Rhombohedral Boron Monosulfide/Ni-Foam Electrodes with Carbon Material

Karin Oiwa,[#] Ryuki Tsuji,[#] Rimpei Ueno, Jinyu Li, Linghui Li, Myu Kawase, Keita Nakayama, Natsumi Noguchi, Susmita Roy, Osamu Oki, Ryotaro Sakakibara, Ken Sakaushi, Masashi Miyakawa, Takashi Taniguchi, and Takahiro Kondo*

Cite This: *ACS Appl. Energy Mater.* 2025, 8, 15186−15195

Read Online

ACCESS | Metrics & More | Article Recommendations | Supporting Information

ABSTRACT: In this study, we systematically investigated the impact of carbon support properties on the oxygen evolution reaction (OER) activity of rhombohedral boron monosulfide (r-BS), a two-dimensional catalyst composed solely of main group elements. Specifically, we examined the effects of crystallinity (crystallite size), defect density (Raman I_D/I_G ratio), and wettability (water contact angle) for four carbon materials: graphene, graphite, carbon black, and multiwalled carbon nanotube (MWCNT). A large number of independent r-BS/carbon material/Ni-foam electrodes were fabricated, and the average current density at 1.8 V vs RHE was evaluated through statistical analysis. The OER activity followed the order: graphene ≈ graphite > carbon black > MWCNT. However, no clear correlation was found with crystallite size or I_D/I_G ratio. In contrast, the contact angle showed a clear inverse relationship with OER activity, with measured values of 0, 55, 99, and 113° for graphene, graphite, carbon black, and MWCNT, respectively. The graphene-based composite showed the highest current density, although with large variability. In contrast, the graphite-based composite demonstrated similarly high activity with significantly better reproducibility. These findings highlight that the hydrophilicity of the carbon support, which governs the detachment of oxygen gas bubbles from the electrode surface, is a dominant factor in high-current-density OER performance. Overall, this study underscores the importance of contact angle engineering as a practical design principle for optimizing nonprecious-metal-based catalyst−support composites.

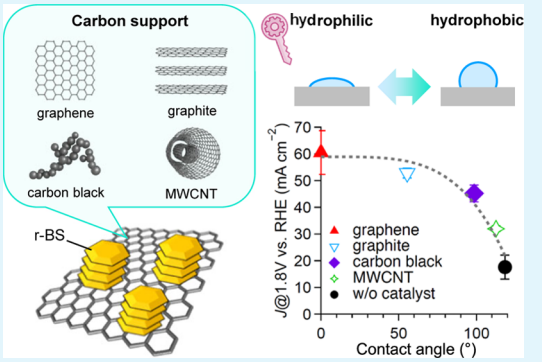

KEYWORDS: *oxygen evolution reaction, water splitting, water electrolysis, wettability, boron sulfide*

INTRODUCTION

Achieving a sustainable society has brought increasing global attention to hydrogen as a clean energy carrier.[1−3] Among various hydrogen production methods, water electrolysis powered by surplus renewable electricity—such as solar and wind—offers a highly stable and environmentally friendly approach.[4,5]

Water electrolysis consists of two half-reactions: the hydrogen evolution reaction (HER) and the oxygen evolution reaction (OER). While HER proceeds via a two-electron transfer process, OER involves a more complex four-electron pathway. As a result, OER is kinetically sluggish and typically becomes the rate-determining step, limiting the overall energy efficiency of electrolysis.[6,7]

To address this, precious metal-based catalysts such as ruthenium oxide (RuO_x) and Iridium oxide (IrO_x) have been extensively studied for their excellent OER activity.[8−10] However, their high cost and scarcity remain significant barriers to large-scale deployment. Therefore, the development of high-performance, nonprecious-metal-based OER electrocatalysts using earth-abundant elements is urgently needed.[11,12]

In recent years, numerous active nonprecious-metal catalysts have been reported.[13−16] Our group has focused on rhombohedral boron monosulfide (r-BS), a layered material composed solely of main group elements, as a promising OER catalyst.[17−19] r-BS features a two-dimensional structure formed by a 1:1 atomic ratio of boron and sulfur.[20,21] Notably, r-BS has demonstrated enhanced OER performance in alkaline media when combined with graphene as a conductive support.[17,18] This finding highlights the critical influence of support materials on overall catalytic activity and emphasizes

Received: July 8, 2025
Revised: October 3, 2025
Accepted: October 7, 2025
Published: October 13, 2025

the importance of rational design in catalyst−support architectures for optimizing OER performance.

A carbon support for OER electrocatalysis must meet several key requirements: (1) high surface area, (2) high electrical conductivity, and (3) appropriate wettability (hydrophilicity). Each of these factors plays a distinct role in determining the overall catalytic performance.

1) A high surface area is essential to suppress the aggregation of catalyst particles, thereby enhancing their dispersion and exposing more active sites.[22,23] This contributes directly to improving OER activity.
2) Electrical conductivity is also critical, especially for semiconductor catalysts such as r-BS.[24] Because these materials have limited intrinsic conductivity, a conductive carbon support is necessary to ensure efficient charge transport during electrolysis.[25,26]
3) More recently, surface wettability has emerged as a crucial factor. It influences the detachment behavior of oxygen bubbles formed during OER. Poor wettability can cause gas bubbles to adhere to the electrode surface, blocking active sites and reducing the effective reaction area.[27,28] This leads to increased transport resistance and deteriorated performance, particularly under high current conditions.

Recent studies across various material systems have underscored the significance of the balance between hydrophilicity and hydrophobicity.[29−36] In particular, the interaction between wettability and bubble dynamics is becoming recognized as a key determinant of OER efficiency.

A recent systematic review by Li et al. highlighted that micro/nanostructuring of electrode surfaces to achieve superaerophobicity can break the three-phase contact line. This drastically reduces bubble departure diameters (to ∼ 50 μm), enabling up to a 60% increase in current density and significantly lowering overpotential under high-current operation, even with the same catalyst.[28]

Iwata et al. reported that controlling wettability by gradually coating porous Ni foam with polytetrafluoroethylene (PTFE) changed the oxygen bubble detachment size from 200 μm to 4.5 mm. As a result, bubble coverage increased from 0.001 to 0.4, and activation overpotential rose from nearly 0 mV to ∼ 30 mV. These findings provided clear quantitative evidence linking wettability to transport loss.[37]

In carbon-based systems, Kirti et al. engineered a carbon−polymer composite electrode by tuning surface roughness and biphasic wettability. They adjusted the contact angle from 48° (hydrophilic) to 92° (hydrophobic), which dramatically decreased the Tafel slope from 147 to 47 mV dec^{-1} and improved the sustainability of steady-state current through more efficient bubble release.[38]

However, the influence of wettability on the OER performance of catalyst−support composites composed of carbon materials and active catalysts has not been systematically explored. In this study, we selected four representative carbon materials—graphene, graphite, carbon black, and multiwalled carbon nanotube (MWCNT)—as supports for the OER catalyst r-BS. Each r-BS−carbon composite was immobilized on a Ni-foam substrate, and their electrochemical performance was evaluated with careful assessment of reproducibility.

Electrochemical measurements showed that r-BS supported on graphene and graphite exhibited significantly higher OER activity, while carbon black and MWCNT-based composites showed reduced performance. Importantly, a clear correlation was observed between OER activity and the wettability of the carbon support, as quantified by contact angle measurements.

These findings indicate that the wettability of the support surface plays a critical role in facilitating the detachment of oxygen gas bubbles during OER, thereby influencing catalytic efficiency. Thus, surface hydrophilicity emerges as a key design parameter in the development of efficient catalyst−support composites for water electrolysis.

RESULTS AND DISCUSSION

We first characterized the structural properties of the carbon materials used in this study: graphene, graphite, carbon black, and MWCNT. Figure 1 shows the X-ray diffraction (XRD) patterns of these materials.

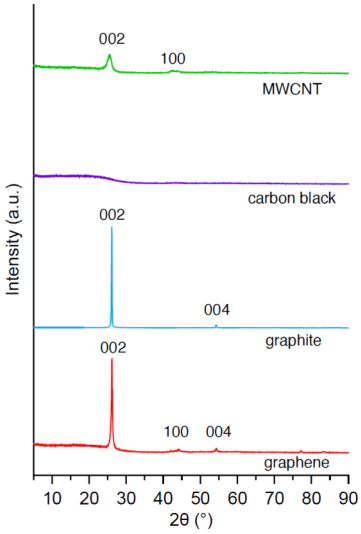

Figure 1. XRD patterns of carbon materials.

For both graphene and graphite, a sharp diffraction peak corresponding to the (002) plane was observed around 26°, indicating a well-ordered layered graphitic structure.[39,40] In contrast, carbon black exhibited no distinct diffraction peaks, suggesting an amorphous or highly disordered structure.[41] The XRD pattern of MWCNT also displayed a peak near 26°, corresponding to the (002) plane, as well as a smaller peak attributed to the 100 plane. These features reflect its multilayered tubular structure derived from stacked graphene sheets.[42]

Crystallite sizes were estimated from the 002 peak using the Scherrer equation.[43] The resulting values were 40.7 nm for graphite, 24.6 nm for graphene, and 4.2 nm for MWCNT. The large crystallite size of graphite, along with its sharp diffraction peak, indicates a highly ordered layer structure. Graphene showed a moderate crystallite size, consistent with its few-layer morphology and expected high dispersibility. MWCNT exhibited the smallest crystallite size, likely due to their short-range stacking and structural heterogeneity. For carbon black, the lack of a well-defined peak prevented estimation of crystallite size.

Next, the Raman spectra of the carbon materials were analyzed, as shown in Figure 2. All samples exhibited characteristic D and G bands in the region of 1300−1600 cm^{-1} (Figure 2a), typical of carbon-based materials. The G

https://doi.org/10.1021/acsaem.5c02078
ACS Appl. Energy Mater. 2025, 8, 15186−15195

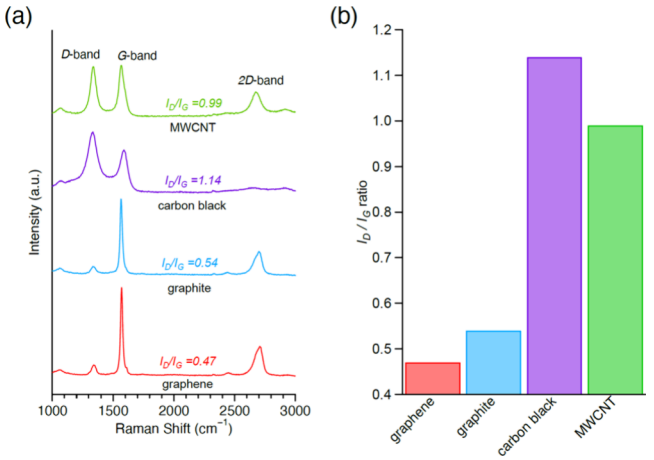

Figure 2. (a) Raman shifts spectra and (b) I_D/I_G ratio of carbon materials.

band (~1580 cm^{-1}) corresponds to the in-plane vibrational mode of sp^2-bonded carbon atoms, associated with graphitic domains and used as an indicator of structural order. In contrast, the D band (~1350 cm^{-1}) arises from lattice defects or disorder and reflects the degree of structural imperfections in the material.[44−47]

Graphene and graphite displayed sharp and intense G bands, indicative of their high crystallinity and low defect density. In contrast, carbon black and MWCNT showed D bands of comparable or even greater intensity than their G bands, suggesting a higher concentration of defects and greater structural disorder. Additionally, MWCNT exhibited a clear 2D band near ~ 2700 cm^{-1}, consistent with the presence of multilayer graphene-like structures.[47]

To quantify the degree of disorder, the intensity ratio of the D to G bands (I_D/I_G) was calculated for each material (Figure 2b).[48] The results showed a distinct trend: graphene (0.47) < graphite (0.54) < MWCNT (0.99) < carbon black (1.14). These values confirm that graphene and graphite possess well-ordered, low-defect structures, whereas carbon black and MWCNT exhibit higher defect densities. Notably, the high I_D/I_G ratio of carbon black is consistent with its amorphous nature, as also indicated by the XRD analysis.

Taken together, the XRD and Raman spectroscopy results reveal clear differences in the structural order and defect levels among the four carbon materials. These intrinsic characteristics are expected to influence interfacial properties with r-BS and potentially impact the performance of the composite electrodes in OER.

Next, composite electrodes were fabricated using r-BS supported on various carbon materials. The r-BS + carbon material catalyst inks were prepared following a previously reported method,[17,18] with graphene, graphite, carbon black, and MWCNT used as the respective carbon supports (Scheme 1a).

To achieve uniform deposition of these inks onto Ni-foam substrates, several modified protocols were evaluated based on existing literature (Figure S2; details provided in the Supporting Information, Experimental Methods). Among the tested methods, the most effective approach involved sonicating the ink followed by gentle manual shaking (Scheme 1b). This method resulted in the most homogeneous and efficient loading of the catalyst onto the Ni-foam surface, as confirmed by optical imaging (Figure S3 and S4), and exhibited the highest OER activity among the tested protocols (Figure S5).

Accordingly, this sonication−shake deposition method was adopted as the standard procedure for fabricating all catalyst-coated electrodes in this study.

Transmission electron microscopy (TEM) was conducted to investigate the morphology of r-BS composites prepared with

Scheme 1. (a) Schematic Illustration of the Preparation Procedure for r-BS + Carbon Materials in Ethanol with Nafion Binder; (b) Schematic Illustration of r-BS + Carbon Material/Ni-Foam (Connected to a Nickel Wire via Spot Welding)

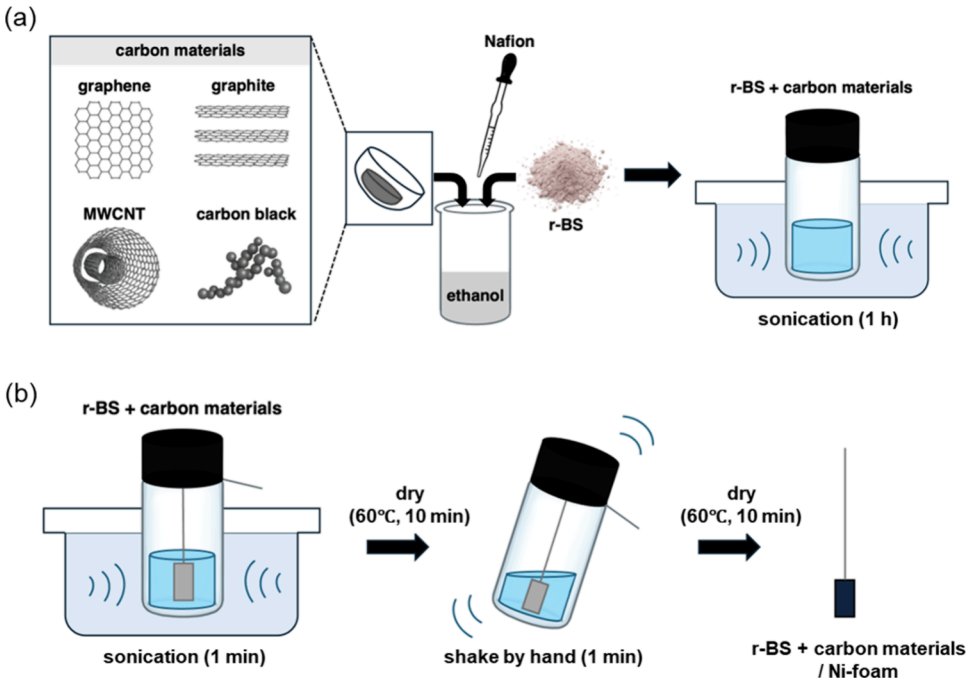

https://doi.org/10.1021/acsaem.5c02078
ACS Appl. Energy Mater. 2025, 8, 15186−15195

various carbon materials, including graphene, graphite, carbon black, and MWCNT (Figure 3a). In the TEM images, r-BS

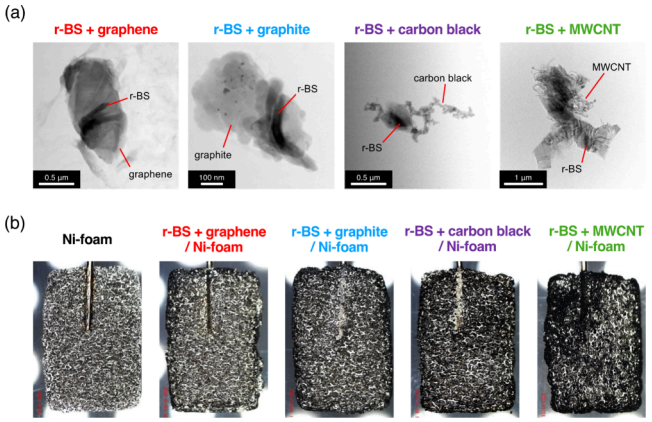

Figure 3. (a) TEM images of r-BS + carbon materials (graphene, graphite, carbon black, and MWCNT). (b) Optical microscope images of r-BS + carbon material/Ni-foam.

appears as darker contrast domains, while the carbon supports typically appear as lighter or more translucent background structures. Distinct differences in dispersion behavior were observed depending on the type of carbon support. These dark r-BS domains are broadly and relatively uniformly spread across the planar carbon sheet structures for graphene and graphite, indicating good dispersion and close surface contact. In contrast, for carbon black and MWCNT, r-BS domains tend to localize in clusters or adhere along curved or entangled structures, showing a less uniform spatial distribution and suggesting a more heterogeneous interfacial interaction. These results indicate that the nature of the carbon support significantly affects the dispersion and interfacial morphology of the r-BS catalyst. For reference, a RuO_2 + graphene composite was also examined, and a similar distribution of RuO_2 particles on the graphene surface was confirmed (Figure S6a).

In addition, optical microscopy was used to assess the macroscopic surface morphology of the r-BS + carbon material/Ni-foam composite electrodes (Figure 3b). Although variations in visual color tone were observed depending on the carbon material—potentially indicating differences in apparent loading—the black catalyst inks were generally well distributed across the Ni-foam substrate. This confirms that uniform coating was achieved regardless of the carbon type. A similar homogeneous distribution was also observed for the RuO_2 + graphene/Ni-foam electrode (Figure S6b), further supporting the reproducibility of the coating process.

To evaluate the elemental distribution on the surface of the composite electrodes, scanning electron microscopy (SEM) combined with energy-dispersive X-ray (EDX) mapping was performed (Figure S7). The EDX maps revealed the presence of C, O, S, and Ni elements across the electrode surface. Notably, the widespread distribution of sulfur confirmed that the r-BS component was uniformly deposited over the Ni-foam substrate. These results are consistent with the optical microscopy observations and support the conclusion that a uniform catalyst coating was successfully achieved for all electrode samples.

Electrochemical measurements were carried out using the prepared r-BS + carbon material/Ni-foam electrodes as the working electrodes. A standard three-electrode cell configuration was assembled, as illustrated in Figure S8. Linear sweep voltammetry (LSV) was conducted to evaluate the OER performance of each sample. The LSV results for all electrode configurations are shown in Figure S9.

To ensure statistical robustness, 27 independent electrodes were fabricated and measured under each condition. Among all samples, the pristine Ni-foam exhibited the lowest current density, reflecting its minimal catalytic activity toward OER (Figure S9a). In contrast, the benchmark catalyst, RuO_2 + graphene/Ni-foam, displayed an earlier onset of current, indicating its superior intrinsic activity (Figure S9b).

For the r-BS-based composite electrodes, the choice of carbon support significantly influenced the electrochemical performance. In particular, r-BS supported on graphene and graphite exhibited markedly higher current densities compared to those supported on carbon black or MWCNT (Figure S9c–f).

Figure 4 summarizes the OER performance of r-BS + carbon material/Ni-foam electrodes, based on the LSV data. Figure 4a presents the average LSV curves derived from the multiple measurements shown in Figure S9, offering a comparative overview of the representative electrochemical behavior for each electrode.

In Figure 4b, the current densities at 1.8 V vs RHE for all individual samples are displayed as violin plots. This visualization captures not only the mean values but also the distribution, variability, and reproducibility of the data—making it a central indicator for evaluating OER performance in this study.

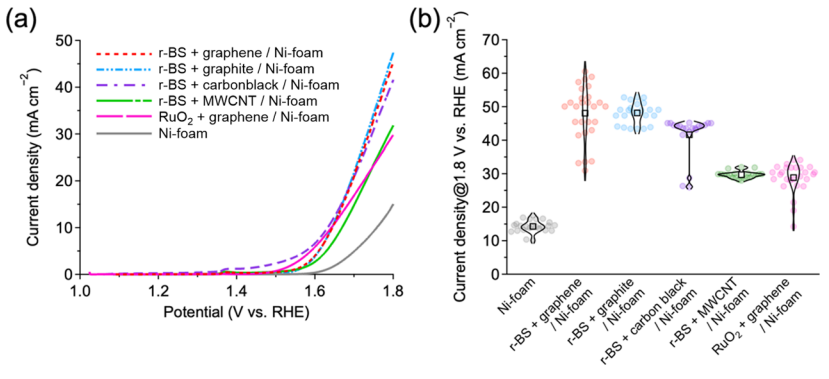

Figure 4. Comparison of the (a) average LSV curves and (b) current density at 1.8 V vs RHE for r-BS + carbon material/Ni-foam.

https://doi.org/10.1021/acsaem.5c02078
ACS Appl. Energy Mater. 2025, 8, 15186−15195

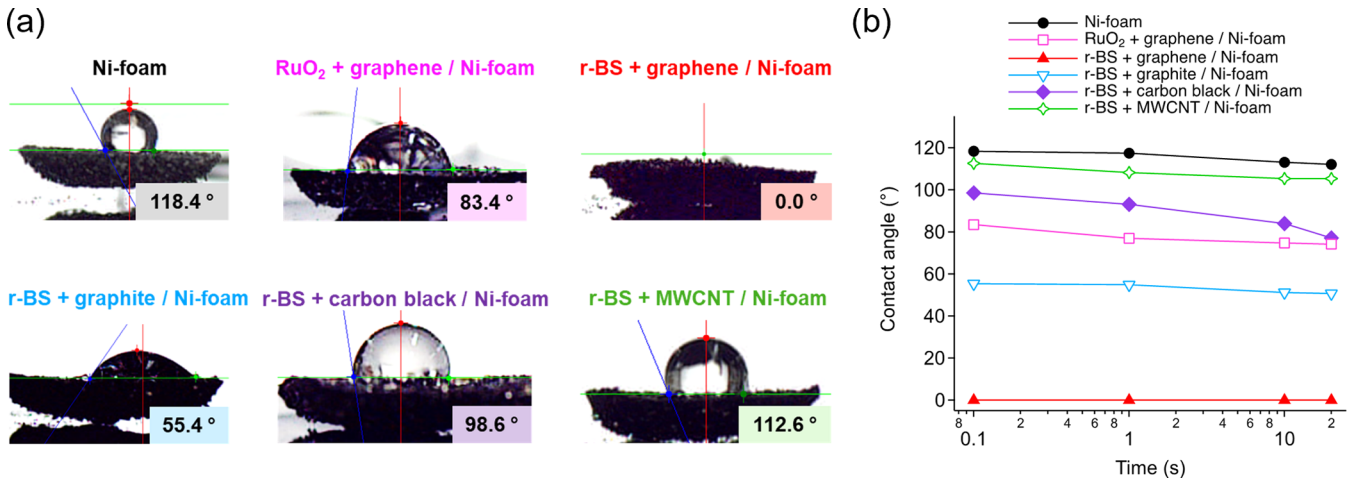

Figure 5. (a) Contact angle images captured at 0.1 s after water droplet deposition onto r-BS + carbon material/Ni-foam during wettability tests. (b) Contact angle variation over time.

The violin plots reveal that the r-BS composites supported on graphene and graphite delivered the highest current densities. Notably, the graphite-supported electrode showed a narrower distribution, reflecting superior reproducibility and stability. In contrast, the graphene-supported electrode achieved the highest peak performance but exhibited greater variability among samples. The carbon black-supported electrode showed moderate activity, while the MWCNT-based composite displayed the lowest current density among the tested materials.

These results clearly indicate that the choice of carbon support significantly affects not only the absolute OER performance, but also its reproducibility.

The RuO_2 + graphene/Ni-foam electrode exhibited an early onset of current, indicating efficient OER initiation at lower potentials (Figure 4a). However, its final current density at 1.8 V vs RHE was lower than that of the r-BS-based composites (Figure 4b), suggesting limited performance in the high-potential region. This trend is consistent with our previous reports, where r-BS-based electrodes outperformed RuO_2-based systems.[17,18]

To provide a clear comparison, the key electrochemical parameters of all tested electrodes, including overpotential at 10 mA cm^{-2}, current density at 1.8 V vs RHE, and Tafel slope, are summarized in Table S1. This table highlights the distinct differences among the carbon-supported r-BS composites and reference electrodes.

In addition, to benchmark the performance of r-BS + carbon/Ni-foam electrodes against previously reported sulfide-based OER catalysts, we compiled the overpotential and Tafel slope values from the literature together with our results (Table S2). This comparison confirms that the r-BS-based composites investigated here exhibit competitive activity relative to other representative metal sulfide systems.

It should be noted that the overall OER activities observed in this study are lower than those reported previously.[17,18] This discrepancy is likely attributed to suboptimal electrode preparation, particularly the lack of optimization in surface wettability (as discussed later) and drying conditions, which may have limited the intrinsic performance of electrocatalysts.

For a more comprehensive evaluation of the catalytic performance, we performed electrochemical impedance spectroscopy (EIS), double-layer capacitance (C_{dl}), and electrochemically active surface area (ECSA) measurements. The Nyquist plots (Figure S13) reveal differences in charge-transfer resistance among the composites. In particular, the r-BS + graphene/Ni-foam electrode exhibited the smallest onset and semicircle diameter, corresponding to the lowest solution series resistance and charge-transfer resistance, respectively, while the r-BS + MWCNT/Ni-foam electrode showed the largest onset and semicircle, indicating sluggish interfacial kinetics.

Cyclic voltammetry in the non-Faradaic region (Figure S14) was used to estimate C_{dl}, and the resulting ECSA values were obtained from the slope of ΔJ versus scan rate (Figure S15). As shown in Figure S15, the carbon black-based electrode displayed the largest ΔJ and consequently the highest apparent ECSA, while graphene- and graphite-supported electrodes exhibited much smaller values. This result clearly indicates that electrochemically accessible surface area alone cannot explain the observed differences in OER activity. Therefore, we considered that other surface-related properties must be involved, and turned our attention to wettability as a possible decisive factor.

In addition to these activity-related factors, we also examined the durability of the r-BS + carbon/Ni-foam electrodes (Figure S16). Although all samples retained activity over 8000 s, the CP curves revealed that the r-BS composites operated at lower potentials than the RuO_2 electrode, indicating that their catalytic activity was sufficiently maintained. The CA profiles showed gradual current variations over time, but overall the r-BS-based electrodes preserved stable operation throughout the test period.

Next, we investigated the wettability of the electrode surfaces, as it is considered one of the key factors influencing the performance differences among the carbon supports.

Figure 5a shows the contact angles measured at 0.1 s after the deposition of a water droplet on the surface of each r-BS + carbon material/Ni-foam electrode. The pristine Ni-foam and the r-BS + MWCNT/Ni-foam electrode exhibited significant hydrophobicity, with contact angles of 118.4° and 112.6°, respectively. In contrast, the electrodes with graphite, carbon black, and MWCNT supports showed contact angles of 55.4°, 98.6°, and 112.6°, respectively, indicating that wettability varies considerably depending on the type of carbon support.

https://doi.org/10.1021/acsaem.5c02078
ACS Appl. Energy Mater. 2025, 8, 15186−15195

Notably, the r-BS + graphene/Ni-foam electrode demonstrated a contact angle of 0°, indicating complete hydrophilicity, with the water droplet spreading immediately across the surface. The RuO_2 + graphene/Ni-foam electrode also exhibited moderate wettability, with a contact angle of 83.4°.

Figure 5b presents the time-dependent variation in contact angle over 20 s after droplet deposition. For all electrodes except the graphene-based one, a slight decrease in contact angle was observed over time. However, the relative order of wettability remained largely unchanged throughout the measurement period. These results confirm that the initial contact angle serves as a reliable indicator of overall surface wettability.

Figure 6 illustrates the relationship between the contact angle and the average current density at 1.8 V vs RHE for each

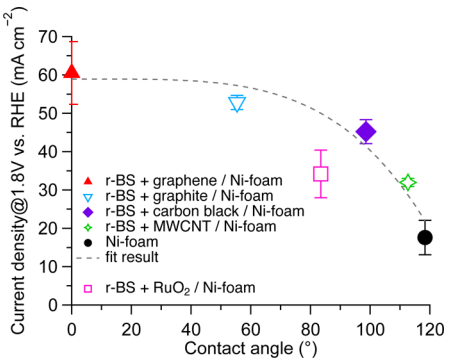

Figure 6. Plot of the relationship between contact angle and average current density at 1.8 V vs RHE for r-BS + carbon material/Ni-foam electrodes. The dashed line represents the fit result. Error bars for the current density indicate the standard deviation derived from the data plotted in Figure 4b.

r-BS + carbon material/Ni-foam electrode. The dashed line in the plot represents the fitted trend based on the measured data for r-BS-based electrodes, excluding the RuO_2 + graphene/Ni-foam benchmark.

Overall, a clear inverse correlation was observed: electrodes with smaller contact angles (i.e., more hydrophilic surfaces) exhibited higher OER current densities. This trend strongly suggests a direct influence of surface wettability on electrocatalytic performance.

In particular, the graphene-supported electrode demonstrated complete hydrophilicity with a contact angle of 0° and simultaneously achieved the highest current density. In contrast, the Ni-foam and MWCNT-based electrodes showed large contact angles exceeding 110°, along with significantly lower current densities. Graphite and carbon black electrodes exhibited intermediate wettability and performance, indicating a continuous dependence of OER activity on surface hydrophilicity.

These findings clearly confirm that the "additional factors" suggested by the ECSA analysis are directly related to surface wettability. These results demonstrate that wettability is not merely a surface property but plays a direct role in determining OER activity. It likely affects both the detachment efficiency of evolved oxygen gas bubbles and the accessibility of hydroxide ions to the catalyst surface. In particular, highly hydrophilic surfaces facilitate rapid O_2 bubble release, thereby maintaining active catalytic sites and enabling sustained, efficient oxygen evolution.

Figure 7a and 7b show the electrode surfaces after water electrolysis. Figure 7a presents the pristine Ni-foam electrode,

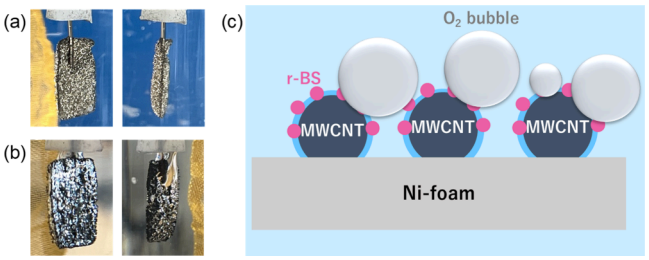

Figure 7. Photographs of sample surfaces after water electrolysis. (a) Ni-foam and (b) r-BS + MWCNT/Ni-foam. Schematic image of O_2 bubbles that do not detach due to the hydrophobicity of the sample surface. (c) Schematic illustration of O_2 bubbles that do not detach due to the hydrophobicity of the sample surface.

while Figure 7b displays the r-BS + MWCNT/Ni-foam electrode following electrolysis in water. In the case of Ni-foam, oxygen bubbles generated during electrolysis detached relatively quickly, and no significant bubble accumulation was observed on the surface. By contrast, the MWCNT-supported electrode exhibited a large number of residual oxygen bubbles that remained adhered to the electrode surface.

Figure 7c provides a schematic illustration of the r-BS + MWCNT/Ni-foam electrode structure and bubble behavior. The MWCNT layer forms a microscopically rough surface on the Ni-foam, imparting a water-repellent nature due to the so-called "lotus effect."[49−52] This micro texture leads to a high degree of surface hydrophobicity.

As a result of this strong hydrophobicity, oxygen bubbles generated during the OER tend to adhere tightly to the electrode surface rather than detaching efficiently. This bubble accumulation can temporarily block active sites on the catalyst surface and hinder the supply of hydroxide ions, both of which contribute to a decline in OER performance.

These findings suggest that surface wettability significantly influences bubble detachment behavior during OER. Consequently, controlling the wettability of electrode surfaces is an important strategy for optimizing catalytic performance in electrochemical systems.

Finally, the representative physicochemical properties of the carbon materials used in this study are discussed in terms of the relationship with their OER performance. As summarized in Table 1, electrical conductivity, specific surface area, and edge density have traditionally been employed as key indicators for evaluating the effectiveness of catalyst supports in literature.[53−56] In this work, we extended this analysis by experimentally determining the crystallite size (via XRD), the I_D/I_G ratio (via Raman spectroscopy, as an inverse indicator of crystallinity), and the water contact angle (at 0.1 s) to systematically evaluate their relationship with OER performance.

In addition, we attempted to obtain the BET surface area of the r-BS + carbon composites. However, as a representative case, the BET analysis of the r-BS + graphene/Ni-foam electrode yielded a negative specific surface area value, indicating that the nitrogen adsorption was too low for reliable determination (Figure S17). This outcome is likely because the catalyst was deposited only on the outer surface of the Ni-foam without forming a sufficiently porous structure. Nevertheless, since electrochemical reactions predominantly occur at the

https://doi.org/10.1021/acsaem.5c02078
ACS Appl. Energy Mater. 2025, 8, 15186−15195

Table 1. Summary of Physicochemical Properties of Carbon Materials Used in This Study[a]

	literature values			experimental values		
carbon materials	electrical conductivity (S/cm)	surface area (m^2/g)	qualitative edge density	crystallite size (nm)	I_D/I_G ratio	contact angle at 0.1 s (°)
graphene	10^3–10^7	1000–3000	moderate	24.6	0.47	0°
graphite	10^1–10^2	1–10	moderate	40.7	0.54	55.4°
carbon black	10^2–10^3	10–1000	high	n.d.	1.14	98.6°
MWCNT	10^4–10^5	100–500	low	4.2	0.99	112.6°

[a]Literature values include electrical conductivity, surface area, and qualitative edge density.[53−56] Experimental values include crystallite size (from XRD), I_D/I_G ratio (from Raman spectroscopy), and water contact angle at 0.1 s.

electrode surface, the absence of bulk porosity is not expected to hinder OER activity. For reference, literature values of the specific surface area for each carbon material are summarized in Table 1.

Graphene exhibited moderate crystallinity (24.6 nm), a low defect density (I_D/I_G = 0.47), and complete hydrophilicity (contact angle = 0°), resulting in the highest OER current density among all materials tested. Graphite also demonstrated high crystallinity (40.7 nm), a relatively low defect density (0.54), and moderate wettability (55.4°), achieving the second-highest OER activity. However, graphite showed better reproducibility in OER performance compared to graphene.

Carbon black, despite its high surface area and edge density, showed low crystallinity (I_D/I_G = 1.14) and poor wettability (contact angle = 98.6°). Consequently, it exhibited only moderate OER performance, likely limited by its hydrophobic nature.

MWCNTs had the smallest crystallite size (4.2 nm), relatively high defect density (I_D/I_G = 0.99), and are known for their high electrical conductivity. However, they displayed the highest contact angle (112.6°), indicating strong hydrophobicity, and recorded the lowest OER activity.

These results suggest that while electronic and structural properties of the carbon materials do influence OER performance to some extent, wettability—particularly under high-current-density conditions—plays a dominant role by controlling oxygen bubble detachment behavior and maintaining reaction continuity.

This insight highlights the critical importance of surface wettability control as a new and effective design parameter for optimizing catalyst−support composites, beyond conventional material property comparisons. For instance, introducing hydrophilic modifiers to defect-free yet hydrophobic materials such as MWCNTs could offer a promising strategy—leveraging their inherent electrical conductivity and corrosion resistance while simultaneously improving oxygen bubble release through enhanced surface wettability. This composite approach may enable the design of advanced catalyst systems that synergistically integrate structural stability with improved gas transport dynamics.

CONCLUSIONS

In this study, we selected rhombohedral boron monosulfide (r-BS), a two-dimensional catalyst composed solely of main-group elements, as a model system. We fabricated a large number of composite electrodes by integrating r-BS with four carbon supports—graphene, graphite, carbon black, and multiwalled carbon nanotube (MWCNT)—that differ in surface wettability. Structural analysis, conductivity measurements, and water contact angle evaluations were conducted to systematically examine the correlation between these material properties and oxygen evolution reaction (OER) performance.

When evaluated at 1.8 V vs RHE, r-BS composites supported on graphene and graphite exhibited the highest average current densities, followed by carbon black and MWCNT. The contact angles measured at 0.1 s were 0° for graphene, 55° for graphite, 99° for carbon black, and 113° for MWCNT. A clear correlation was observed between the contact angle and the OER current density.

This behavior, which cannot be explained solely by differences in surface area or electrical conductivity, clearly demonstrates that the hydrophilicity of the support—governing the detachment of oxygen gas bubbles—is the dominant factor in high-current-density OER performance.

Therefore, surface modification and support selection based on contact angle should be regarded as a top-priority strategy for the rational design and optimization of nonprecious-metal-based catalyst−support composites.

ASSOCIATED CONTENT

Supporting Information

The Supporting Information is available free of charge at https://pubs.acs.org/doi/10.1021/acsaem.5c02078.

Experimental methods, supplementary text, Figures S1–S17, and Tables S1 and S2 (PDF)

AUTHOR INFORMATION

Corresponding Author

Takahiro Kondo − *Department of Materials Science, Institute of Pure and Applied Sciences, University of Tsukuba, Tsukuba, Ibaraki 305-8573, Japan; Hydrogen Boride Research Center, Tsukuba Institute of Advanced Research, University of Tsukuba, Tsukuba, Ibaraki 305-8577, Japan; Research Center for Energy and Environmental Materials, National Institute for Materials Science, Tsukuba, Ibaraki 305-0044, Japan; The Advanced Institute for Materials Research, Tohoku University, Sendai, Miyagi 980-8577, Japan;* orcid.org/0000-0001-8457-9387; Email: takahiro@ims.tsukuba.ac.jp

Authors

Karin Oiwa − *Graduate School of Science and Technology, University of Tsukuba, Tsukuba, Ibaraki 305-8574, Japan*

Ryuki Tsuji − *Department of Materials Science, Institute of Pure and Applied Sciences, University of Tsukuba, Tsukuba, Ibaraki 305-8573, Japan; Hydrogen Boride Research Center, Tsukuba Institute of Advanced Research, University of Tsukuba, Tsukuba, Ibaraki 305-8577, Japan*

Rimpei Ueno − *Hydrogen Boride Research Center, Tsukuba Institute of Advanced Research, University of Tsukuba, Tsukuba, Ibaraki 305-8577, Japan*

https://doi.org/10.1021/acsaem.5c02078
ACS Appl. Energy Mater. 2025, 8, 15186−15195

Jinyu Li − *Hydrogen Boride Research Center, Tsukuba Institute of Advanced Research, University of Tsukuba, Tsukuba, Ibaraki 305-8577, Japan*
Linghui Li − *Hydrogen Boride Research Center, Tsukuba Institute of Advanced Research, University of Tsukuba, Tsukuba, Ibaraki 305-8577, Japan*
Myu Kawase − *Hydrogen Boride Research Center, Tsukuba Institute of Advanced Research, University of Tsukuba, Tsukuba, Ibaraki 305-8577, Japan*
Keita Nakayama − *Hydrogen Boride Research Center, Tsukuba Institute of Advanced Research, University of Tsukuba, Tsukuba, Ibaraki 305-8577, Japan*
Natsumi Noguchi − *Hydrogen Boride Research Center, Tsukuba Institute of Advanced Research, University of Tsukuba, Tsukuba, Ibaraki 305-8577, Japan*
Susmita Roy − *Department of Materials Science, Institute of Pure and Applied Sciences, University of Tsukuba, Tsukuba, Ibaraki 305-8573, Japan*
Osamu Oki − *Department of Materials Science, Institute of Pure and Applied Sciences, University of Tsukuba, Tsukuba, Ibaraki 305-8573, Japan; Hydrogen Boride Research Center, Tsukuba Institute of Advanced Research, University of Tsukuba, Tsukuba, Ibaraki 305-8577, Japan*
Ryotaro Sakakibara − *Research Center for Materials Nanoarchitectonics, National Institute for Materials Science, Tsukuba, Ibaraki 305-0044, Japan;* orcid.org/0000-0001-7150-2831
Ken Sakaushi − *Department of Materials Science, Institute of Pure and Applied Sciences, University of Tsukuba, Tsukuba, Ibaraki 305-8573, Japan; Research Center for Energy and Environmental Materials, National Institute for Materials Science, Tsukuba, Ibaraki 305-0044, Japan;* orcid.org/0000-0003-4797-9087
Masashi Miyakawa − *Research Center for Materials Nanoarchitectonics, National Institute for Materials Science, Tsukuba, Ibaraki 305-0044, Japan;* orcid.org/0000-0002-0838-8156
Takashi Taniguchi − *Research Center for Materials Nanoarchitectonics, National Institute for Materials Science, Tsukuba, Ibaraki 305-0044, Japan;* orcid.org/0000-0002-1467-3105

Complete contact information is available at: https://pubs.acs.org/10.1021/acsaem.5c02078

Author Contributions

[#]K.O. and R.T. contributed equally to this work.

Notes

The authors declare no competing financial interest.

■ ACKNOWLEDGMENTS

This work was supported by JST A-step Program Japan (grant no. JPMJTR22T4), JSPS KAKENHI (grant nos. JP21H00015:B01, JP21H05012, JP22K18964, JP23H01843, JP23K26536, JP24H02204, and JP25K22213), GteX Program Japan (grant nos. JPMJGX23H2 and JPMJGX23H1), and Sumitomo Electric Industries, Ltd. The authors gratefully acknowledge Keisuke Shinoda (NIMS) for his support with the TEM observations.

■ REFERENCES

(1) Staffell, I.; Scamman, D.; Velazquez Abad, A.; Balcombe, P.; Dodds, P. E.; Ekins, P.; Shah, N.; Ward, K. R. The Role of Hydrogen and Fuel Cells in the Global Energy System. *Energy Environ. Sci.* **2019**, *12*, 463−491.
(2) Kovač, A.; Paranos, M.; Marciuš, D. Hydrogen in Energy Transition: A Review. *Int. J. Hydrogen Energy* **2021**, *46* (16), 10016−10035.
(3) Dincer, I. Hydrogen 1.0: A New Age. *Int. J. Hydrogen Energy* **2023**, *48* (43), 16143−16147.
(4) Oliveira, A. M.; Beswick, R. R.; Yan, Y. A Green Hydrogen Economy for a Renewable Energy Society. *Curr. Opin. Chem. Eng.* **2021**, *33*, No. 100701.
(5) Amin, M.; Shah, H. H.; Fareed, A. G.; Khan, W. U.; Chung, E.; Zia, A.; Rahman Farooqi, Z. U.; Lee, C. Hydrogen Production through Renewable and Non-Renewable Energy Processes and Their Impact on Climate Change. *Int. J. Hydrogen Energy* **2022**, *47* (77), 33112−33134.
(6) Wang, X.; Zhong, H.; Xi, S.; Lee, W. S. V.; Xue, J. Understanding of Oxygen Redox in the Oxygen Evolution Reaction. *Adv. Mater.* **2022**, *34* (50), No. 2107956.
(7) Xie, X.; Du, L.; Yan, L.; Park, S.; Qiu, Y.; Sokolowski, J.; Wang, W.; Shao, Y. Oxygen Evolution Reaction in Alkaline Environment: Material Challenges and Solutions. *Adv. Funct. Mater.* **2022**, *32* (21), No. 2110036.
(8) Qin, R.; Chen, G.; Feng, X.; Weng, J.; Han, Y. Ru/Ir-Based Electrocatalysts for Oxygen Evolution Reaction in Acidic Conditions: From Mechanisms, Optimizations to Challenges. *Adv. Sci.* **2024**, *11* (21), No. 2309364.
(9) Spöri, C.; Briois, P.; Nong, H. N.; Reier, T.; Billard, A.; Kühl, S.; Teschner, D.; Strasser, P. Experimental Activity Descriptors for Iridium-Based Catalysts for the Electrochemical Oxygen Evolution Reaction (OER). *ACS Catal.* **2019**, *9* (8), 6653−6663.
(10) Tsuji, R.; Koshino, Y.; Masutani, H.; Haruyama, Y.; Niibe, M.; Suzuki, S.; Nakashima, S.; Fujisawa, H.; Ito, S. Water Electrolysis Using Thin Pt and RuOx Catalysts Deposited by a Flame-Annealing Method on Pencil-Lead Graphite-Rod Electrodes. *ACS Omega* **2020**, *5* (11), 6090−6099.
(11) Shi, Q.; Zhu, C.; Du, D.; Lin, Y. Robust Noble Metal-Based Electrocatalysts for Oxygen Evolution Reaction. *Chem. Soc. Rev.* **2019**, *48*, 3181−3192.
(12) Wu, Z. P.; Lu, X. F.; Zang, S. Q.; Lou, X. W. Non-Noble-Metal-Based Electrocatalysts toward the Oxygen Evolution Reaction. *Adv. Funct. Mater.* **2020**, *30* (15), No. 1910274.
(13) Chen, Y.; Li, Q.; Lin, Y.; Liu, J.; Pan, J.; Hu, J.; Xu, X. Boosting Oxygen Evolution Reaction by FeNi Hydroxide-Organic Framework Electrocatalyst toward Alkaline Water Electrolyzer. *Nat. Commun.* **2024**, *15* (1), 7278.
(14) Rafiq, M.; Harrath, K.; Feng, M.; Li, R.; Woldu, A. R.; Chu, P. K.; Hu, L.; Lu, F.; Yao, X. $Ni_xB/Mo_{0.8}B_3$ Nanorods Encapsulated by a Boron-Rich Amorphous Layer for Universal PH Water Splitting at the Ampere Level. *Adv. Energy. Mater.* **2024**, *14* (45), No. 2402866.
(15) Zahran, Z. N.; Mohamed, E. A.; Tsubonouchi, Y.; Ishizaki, M.; Togashi, T.; Kurihara, M.; Saito, K.; Yui, T.; Yagi, M. Electrocatalytic Water Splitting with Unprecedentedly Low Overpotentials by Nickel Sulfide Nanowires Stuffed into Carbon Nitride Scabbards. *Energy Environ. Sci.* **2021**, *14* (10), 5358−5365.
(16) Arcas, R.; Koshino, Y.; Mas-Marzá, E.; Tsuji, R.; Masutani, H.; Miura-Fujiwara, E.; Haruyama, Y.; Nakashima, S.; Ito, S.; Fabregat-Santiago, F. Pencil Graphite Rods Decorated with Nickel and Nickel-Iron as Low-Cost Oxygen Evolution Reaction Electrodes. *Sustain. Energy Fuels* **2021**, *5* (15), 3929−3938.
(17) Li, L.; Hagiwara, S.; Jiang, C.; Kusaka, H.; Watanabe, N.; Fujita, T.; Kuroda, F.; Yamamoto, A.; Miyakawa, M.; Taniguchi, T.; Hosono, H.; Otani, M.; Kondo, T. Boron Monosulfide as an Electrocatalyst for the Oxygen Evolution Reaction. *Chem. Eng. J.* **2023**, *471*, No. 144489.
(18) Li, L.; Watanabe, N.; Jiang, C.; Yamamoto, A.; Fujita, T.; Miyakawa, M.; Taniguchi, T.; Hosono, H.; Kondo, T. Development of a Highly Stable Nickel-Foam-Based Boron Monosulfide−Graphene Electrocatalyst with a High Current Density for the Oxygen Evolution Reaction. *Sci. Technol. Adv. Mater.* **2023**, *24* (1), No. 2277681.

(19) Hagiwara, S.; Kuroda, F.; Kondo, T.; Otani, M. Electrocatalytic Mechanisms for an Oxygen Evolution Reaction at a Rhombohedral Boron Monosulfide Electrode/Alkaline Medium Interface. *ACS Appl. Mater. Interfaces* **2023**, *15* (43), 50174−50184.
(20) Sasaki, T.; Takizawa, H.; Uheda, K.; Endo, T. High Pressure Synthesis of Binary B-S Compounds. *Phys. Status Solidi B* **2001**, *223* (1), 29−33.
(21) Kusaka, H.; Ishibiki, R.; Toyoda, M.; Fujita, T.; Tokunaga, T.; Yamamoto, A.; Miyakawa, M.; Matsushita, K.; Miyazaki, K.; Li, L.; Shinde, S. L.; Lima, M. S. L.; Sakurai, T.; Nishibori, E.; Masuda, T.; Horiba, K.; Watanabe, K.; Saito, S.; Miyauchi, M.; Taniguchi, T.; Hosono, H.; Kondo, T. Crystalline Boron Monosulfide Nanosheets with Tunable Bandgaps. *J. Mater. Chem. A* **2021**, *9* (43), 24631−24640.
(22) Sun, S.; Li, H.; Xu, Z. J. Impact of Surface Area in Evaluation of Catalyst Activity. *Joule* **2018**, *2* (6), 1024−1027.
(23) Wu, T.; Han, M. Y.; Xu, Z. J. Size Effects of Electrocatalysts: More Than a Variation of Surface Area. *ACS Nano* **2022**, *16* (6), 8531−8539.
(24) Watanabe, N.; Miyazaki, K.; Toyoda, M.; Takeyasu, K.; Tsujii, N.; Kusaka, H.; Yamamoto, A.; Saito, S.; Miyakawa, M.; Taniguchi, T.; Aizawa, T.; Mori, T.; Miyauchi, M.; Kondo, T. Rhombohedral Boron Monosulfide as a P-Type Semiconductor. *Molecules* **2023**, *28* (4), 1896.
(25) Zou, S.; Burke, M. S.; Kast, M. G.; Fan, J.; Danilovic, N.; Boettcher, S. W. Fe (Oxy)Hydroxide Oxygen Evolution Reaction Electrocatalysis: Intrinsic Activity and the Roles of Electrical Conductivity, Substrate, and Dissolution. *Chem. Mater.* **2015**, *27* (23), 8011−8020.
(26) Zhao, X.; Zhang, H.; Yan, Y.; Cao, J.; Li, X.; Zhou, S.; Peng, Z.; Zeng, J. Engineering the Electrical Conductivity of Lamellar Silver-Doped Cobalt(II) Selenide Nanobelts for Enhanced Oxygen Evolution. *Angew. Chem., Int. Ed.* **2017**, *56* (1), 328−332.
(27) Dastafkan, K.; Li, Y.; Zeng, Y.; Han, L.; Zhao, C. Enhanced Surface Wettability and Innate Activity of an Iron Borate Catalyst for Efficient Oxygen Evolution and Gas Bubble Detachment. *J. Mater. Chem. A* **2019**, *7* (25), 15252−15261.
(28) Li, M.; Xie, P.; Yu, L.; Luo, L.; Sun, X. Bubble Engineering on Micro-/Nanostructured Electrodes for Water Splitting. *ACS Nano* **2023**, *17* (23), 23299−23316.
(29) Li, Y.; Zhao, C. Enhancing Water Oxidation Catalysis on a Synergistic Phosphorylated NiFe Hydroxide by Adjusting Catalyst Wettability. *ACS Catal.* **2017**, *7* (4), 2535−2541.
(30) Wang, R.; Jiang, W.; Xia, D.; Liu, T.; Gan, L. Improving the Wettability of Thin-Film Rotating Disk Electrodes for Reliable Activity Evaluation of Oxygen Electrocatalysts by Triggering Oxygen Reduction at the Catalyst-Electrolyte-Bubble Triple Phase Boundaries. *J. Electrochem. Soc.* **2018**, *165* (7), F436−F440.
(31) Liu, G.; Wu, Y.; Wang, M.; Yao, R.; Li, N.; Zhao, Y.; Zhao, F.; Li, J. Phosphate Ions-Functionalized and Wettability-Tuned Nickel Ferrite for Boosted Oxygen Evolution Performance. *Int. J. Hydrogen Energy* **2019**, *44* (49), 26992−27000.
(32) Fujimura, T.; Hikima, W.; Fukunaka, Y.; Homma, T. Analysis of the Effect of Surface Wettability on Hydrogen Evolution Reaction in Water Electrolysis Using Micro-Patterned Electrodes. *Electrochem. commun.* **2019**, *101*, 43−46.
(33) Kim, J.; Jung, S. M.; Lee, N.; Kim, K. S.; Kim, Y. T.; Kim, J. K. Efficient Alkaline Hydrogen Evolution Reaction Using Super-aerophobic Ni Nanoarrays with Accelerated H_2 Bubble Release. *Adv. Mater.* **2023**, *35* (52), No. 2305844.
(34) Jiang, W.; Huang, X.; Ke, W.; Sheng, L.; Li, J. J.; Zhu, F.; Cheng, W.; Zhang, Z.; Lao, Y.; Chen, Y. Tuning Wettability of Nickel-Based Electrode by Micro-Nano Surface Structure to Boost OER Catalysis. *J. Alloys Compd.* **2023**, *965*, No. 171367.
(35) Shao, X.; Li, D.; Zhou, A.; Zhu, L.; Du, Y.; Li, B.; Zhang, Y.; Cao, L.; Yang, J. Superhydrophilic $CoMoO_4$ with High Oxygen Vacancy for Outstanding Alkaline OER. *Int. J. Hydrogen Energy* **2024**, *58*, 1284−1294.
(36) Zhu, F.; Wen, X.; Li, X.; Wang, Y.; Shao, K.; Shen, S.; Zhao, X. Tuning the Wettability of Binary Alloy Electrodes to Promote OER Catalysis in Alkaline Media by Group Distribution Ratio. *ACS Appl. Energy Mater.* **2025**, *8* (2), 1210−1219.
(37) Iwata, R.; Zhang, L.; Wilke, K. L.; Gong, S.; He, M.; Gallant, B. M.; Wang, E. N. Bubble Growth and Departure Modes on Wettable/Non-Wettable Porous Foams in Alkaline Water Splitting. *Joule* **2021**, *5* (4), 887−900.
(38) Kirti; Nandha, N.; Singh, P. S.; Srivastava, D. N. Improved OER Performance on the Carbon Composite Electrode through Tailored Wettability. *ACS Appl. Energy Mater.* **2021**, *4* (9), 9618−9626.
(39) Li, Z. Q.; Lu, C. J.; Xia, Z. P.; Zhou, Y.; Luo, Z. X-Ray Diffraction Patterns of Graphite and Turbostratic Carbon. *Carbon* **2007**, *45* (8), 1686−1695.
(40) Bogachuk, D.; Tsuji, R.; Martineau, D.; Narbey, S.; Herterich, J. P.; Wagner, L.; Suginuma, K.; Ito, S.; Hinsch, A. Comparison of Highly Conductive Natural and Synthetic Graphites for Electrodes in Perovskite Solar Cells. *Carbon* **2021**, *178*, 10−18.
(41) Pawlyta, M.; Rouzaud, J. N.; Duber, S. Raman Microspectroscopy Characterization of Carbon Blacks: Spectral Analysis and Structural Information. *Carbon* **2015**, *84* (1), 479−490.
(42) Singh, D. K.; Iyer, P. K.; Giri, P. K. Diameter Dependence of Interwall Separation and Strain in Multiwalled Carbon Nanotubes Probed by X-Ray Diffraction and Raman Scattering Studies. *Diam. Relat. Mater.* **2010**, *19* (10), 1281−1288.
(43) He, K.; Chen, N.; Wang, C.; Wei, L.; Chen, J. Method for Determining Crystal Grain Size by X-Ray Diffraction. *Cryst. Res. Technol.* **2018**, *53* (2), No. 1700157.
(44) Malard, L. M.; Pimenta, M. A.; Dresselhaus, G.; Dresselhaus, M. S. Raman Spectroscopy in Graphene. *Phys. Rep.* **2009**, *473* (5−6), 51−87.
(45) Reich, S.; Thomsen, C. Raman Spectroscopy of Graphite. *Philos. Trans. R. Soc., A* **2004**, *362* (1824), 2271−2288.
(46) Tsuji, R.; Masutani, H.; Haruyama, Y.; Niibe, M.; Suzuki, S.; Honda, S. I.; Matsuo, Y.; Heya, A.; Matsuo, N.; Ito, S. Water Electrolysis Using Flame-Annealed Pencil-Graphite Rods. *ACS Sustain. Chem. Eng.* **2019**, *7* (6), 5681−5689.
(47) Bokobza, L.; Bruneel, J. L.; Couzi, M. Raman Spectroscopic Investigation of Carbon-Based Materials and Their Composites. Comparison between Carbon Nanotubes and Carbon Black. *Chem. Phys. Lett.* **2013**, *590*, 153−159.
(48) Dresselhaus, M. S.; Jorio, A.; Souza Filho, A. G.; Saito, R. Defect Characterization in Graphene and Carbon Nanotubes Using Raman Spectroscopy. *Philos. Trans. R. Soc., A* **2010**, *368* (1932), 5355−5377.
(49) Marmur, A. The Lotus Effect: Superhydrophobicity and Metastability. *Langmuir* **2004**, *20* (9), 3517−3519.
(50) Wang, P.; Zhao, T.; Bian, R.; Wang, G.; Liu, H. Robust Superhydrophobic Carbon Nanotube Film with Lotus Leaf Mimetic Multiscale Hierarchical Structures. *ACS Nano* **2017**, *11* (12), 12385−12391.
(51) Yamamoto, M.; Nishikawa, N.; Mayama, H.; Nonomura, Y.; Yokojima, S.; Nakamura, S.; Uchida, K. Theoretical Explanation of the Lotus Effect: Superhydrophobic Property Changes by Removal of Nanostructures from the Surface of a Lotus Leaf. *Langmuir* **2015**, *31* (26), 7355−7363.
(52) Liu, Y.; Tang, J.; Wang, R.; Lu, H.; Li, L.; Kong, Y.; Qi, K.; Xin, J. H. Artificial Lotus Leaf Structures from Assembling Carbon Nanotubes and Their Applications in Hydrophobic Textiles. *J. Mater. Chem.* **2007**, *17* (11), 1071−1078.
(53) Garg, R.; Rastogi, S. K.; Lamparski, M.; De La Barrera, S. C.; Pace, G. T.; Nuhfer, N. T.; Hunt, B. M.; Meunier, V.; Cohen-Karni, T. Nanowire-Mesh-Templated Growth of Out-of-Plane Three-Dimensional Fuzzy Graphene. *ACS Nano* **2017**, *11* (6), 6301−6311.
(54) Ikram, R.; Jan, B. M.; Pervez, S. A.; Papadakis, V. M.; Ahmad, W.; Bushra, R.; Kenanakis, G.; Rana, M. Recent Advancements of N-Doped Graphene for Rechargeable Batteries: A Review. *Crystals* **2020**, *10* (12), 1080.

https://doi.org/10.1021/acsaem.5c02078
ACS Appl. Energy Mater. 2025, 8, 15186−15195

(55) Mirzaeian, M.; Abbas, Q.; Ogwu, A.; Hall, P.; Goldin, M.; Mirzaeian, M.; Jirandehi, H. F. Electrode and Electrolyte Materials for Electrochemical Capacitors. *Int. J. Hydrogen Energy* **2017**, *42* (40), 25565−25587.
(56) Ishii, T.; Kaburagi, Y.; Yoshida, A.; Hishiyama, Y.; Oka, H.; Setoyama, N.; Ozaki, J. I.; Kyotani, T. Analyses of Trace Amounts of Edge Sites in Natural Graphite, Synthetic Graphite and High-Temperature Treated Coke for the Understanding of Their Carbon Molecular Structures. *Carbon* **2017**, *125*, 146−155.

https://doi.org/10.1021/acsaem.5c02078
ACS Appl. Energy Mater. 2025, 8, 15186−15195